Journal of the European Ceramic Society 37 (2017) 2795–2801

Contents lists available at www.sciencedirect.com

Journal of the European Ceramic Society

journal homepage: www.elsevier.com/locate/jeurceramsoc

How to extract reliable core-volume fractions from core-shell polycrystalline microstructures using cross sectional TEM micrographs

F.H. Morshead, P.Y. Foeller, C.L. Freeman, H. Zhang, I.M. Reaney, D.C. Sinclair, J.S. Dean *

Department of Materials Science and Engineering, University of Sheffield, Sheffield S1 3JD, UK

ARTICLE INFO

Article history:
Received 21 January 2017
Received in revised form 1 March 2017
Accepted 2 March 2017
Available online 18 March 2017

ABSTRACT

A reliable method of extracting core-volume fraction from TEM micrographs of core-shell polycrystalline microstructures is presented. Three commonly used averaging methods based on a simple spherical model are shown to consistently underestimate the core-volume fraction due to the interpretation of a 3D structure from a 2D slice. The same trend is also revealed using Voronoi tessellated structures to mimic polycrystalline ceramics. In some cases the underestimate is less than half the true core-volume fraction.

We show that using a new maximum core-volume fraction methodology can improve the extracted value to a consistent error of less than 5%. This approach uses a value taken from the largest core-volume fraction measured from 10 grains that exhibit a core-shell microstructure. This provides increasing accuracy and improvements in the confidence of the measurement when extracting core-volume fractions of polycrystalline ceramics from 2D TEM micrographs.

1. Introduction

Multilayer Ceramic Capacitors (MLCCs) are the building blocks in modern electronics, comprising approximately 30% of the total passive elements in a typical hybrid circuit module [1]. The demand for high performance MLCCs is increasing annually for various applications, including computing, automotive, aerospace and cellular communication. It is estimated that 3 trillion MLCCs/year will be made by 2020 [2]. This $10 billon global market [3], with an estimated 2 trillion units sold in 2015 [4], uses ferroelectric perovskite-based $BaTiO_3$ (BT) at its cornerstone dielectric material due to its high relative permittivity (ε_r) near room temperature. In its un-doped form, the ε_r of BT varies from ~ 1700 at room temperature to over 10,000 near the ferro to para electric transition (T_c~125 °C); consequently it is unusable in modern consumer electronics that require stable capacitance across common operational temperature ranges, e.g. <±15% between −55 and +125 °C for XR7 applications [5].

BT ceramics are chemically doped to achieve temperature stable ε_r profiles for commercial applications. To achieve this, a wide range of additives particularly rare earth elements [6–9] are used. By careful control of the volumetric ratio of un-doped to doped BT, the temperature stability of the capacitance for a BT-based capacitor can be tuned and optimised [10–12]. While some methods now try to use a layered approach (e.g. bilayers or multilayers with different compositions) to reach the optimal volumetric ratio [12,13], conventional ceramic processing is designed to create limited diffusion of the dopants into un-doped BT grains to create a heterogeneous distribution of a 'core-shell' type microstructure within a single ceramic layer. In its simplest form, the sub-grain microstructure consists of a grain-core based on un-doped BT surrounded by an outer-shell grain region with a distribution of dopant(s) that suppress and smear out T_c to lower temperatures. Core-shell microstructures therefore create a much broader ε_r temperature (ε_r–T) profile as compared to un-doped $BaTiO_3$ ceramics and are suitable for a variety of commercial MLCC applications.

As the core and shell regions possess unique electrical characteristics the overall ε_r–T profile depends on many processing and compositional parameters, including grain size, dopant concentrations and distributions, sintering temperature and dwell times and oxygen partial pressure. To achieve optimisation, a trial and error iterative method is commonly employed which has produced a large body of knowledge on RE-doped BT-based MLCC technology. The drive towards higher operating temperatures and reduction in

* Corresponding author.

http://dx.doi.org/10.1016/j.jeurceramsoc.2017.03.006

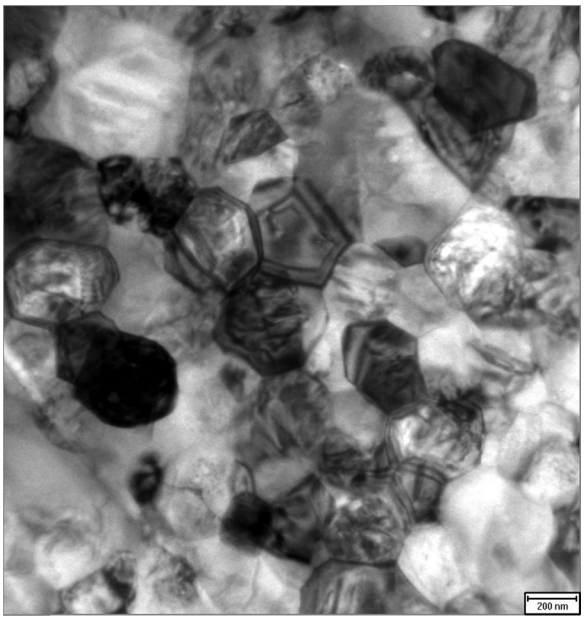

Fig. 1. Bright field image of a doped BT ceramic layer within a MLCC device. A number of core-shell structured grains can be observed.

the use of RE oxides, however, requires the development of new (RE-free) formulations, which, given the lack of iterative data at the disposal of researchers, is challenging to major manufacturers. An understanding of how the core-volume fraction is modified during processing is thus of critical importance for not only improving present generation MLCCs but also incorporating next generation, RE-free material alternatives.

Core and shell volume fractions can be obtained from the electrical response of BT-based ceramics by extracting the capacitance ratio of the regions using impedance spectroscopy [14,15]. For this approach to be successful, the core and shell microstructural regions must have time constants that differ by ~2 orders of magnitude to obtain well resolved impedance responses. Unfortunately, the time constants often differ by less than 2 orders of magnitude and this results in overlapping impedance responses that can be problematic to de-convolute into individual core and shell elements. Furthermore, analysis is commonly based on a brick-work layer model that assumes a homogeneous current flow through both regions [16,17]. Recently, finite element modelling [17] has shown heterogeneous current density pathways can arise from various core-shell microstructured ceramics and this can limit the use of impedance spectroscopy to obtain accurate capacitance values and thus core and shell volume fractions.

While advances in tomography allow direct three-dimensional (3D) imaging of ceramic microstructures [18–20], these techniques are not routinely available and are time-consuming and expensive meaning they are rarely used for this type of characterisation. An alternative, more accessible method is to use high-resolution bright field transmission electron microscopy (TEM) [6,11,21–25]. While this is also resource intensive, requiring expensive equipment, expertise in sample preparation and data collection it does allow the core-shell volumetric ratio to be interrogated directly from 2D micrographs either visually and/or by measuring compositional changes using energy-dispersive X-ray spectroscopy (EDX) [6,11,21–25].

There have been many studies on the influence of the core-shell volumetric ratio on the ε_r–T profile using such approaches [6,9,11,21–23,26–28]. Joen *et al.* [11] used a systematic approach in ceramic processing to alter the core-shell volumetric ratio. They concluded the optimised ε_r–T profile could be obtained in their

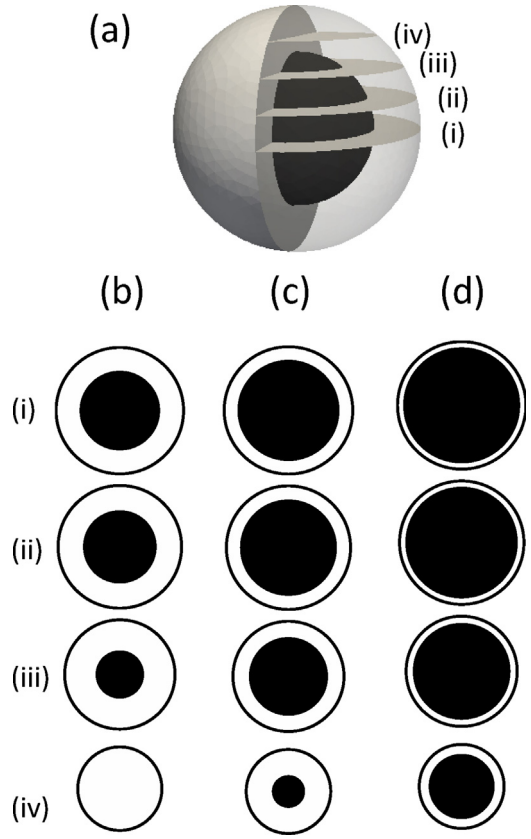

Fig. 2. Schematic spherical model with chords (i) to (iv) used to create 2D sliced images based on three different core-volume fraction (V_{Cf}) structures. (a) A cut away schematic for V_{Cf} = 0.5 (1:1 ratio) highlights the core (black) and shell (white). Four chord intersects are used, set at a distance of (i) 0.00, (ii) 0.25, (iii) 0.50 and (iv) 0.75 μm. Figures (b)–(d) provide the 2D slices of these chord placements for V_{Cf} = 0.25 (b), 0.50 (c) and 0.75 (d).

materials for a core-shell volumetric ratio of ~ 0.3, i.e. the core-volume fraction (un-doped BT) made up 33% of the total grain volume. Their study was performed using direct imaging of the core and shell regions from TEM micrographs along with an EDX study of the compositional gradients of dopants in the shell regions. The core and shell thicknesses were obtained by averaging across many grains which is common practice, as evidenced by existing literature relating to core-shell volumetric ratio [6,11,23–25]. In this article we test the accuracy of this and other common approaches.

To provide clarity, the core-volume fraction V_{Cf} is defined as the core volume V_c divided by the total grain volume V_g as shown in Eq. (1)

$$V_{Cf} = \frac{V_c}{V_g} \tag{1}$$

The shell volume V_s can then be extracted as

$$V_s = V_g - V_c \tag{2}$$

The core-shell volumetric ratio can then be determined, however, for simplicity we will refer only to the core-volume fraction, V_{Cf}.

A typical TEM micrograph from a single layer of BT-based ceramic within a commercial MLCC is shown in Fig. 1. The layer consists of approximately 30 individual grains of which 15 display a core-shell microstructure. Typically, the fact that not all grains show a core-shell structure is ignored or attributed to insufficient imaging or deficiencies in the materials processing. The grains that do exhibit a core-shell structure can then be measured to estimate V_{Cf}.

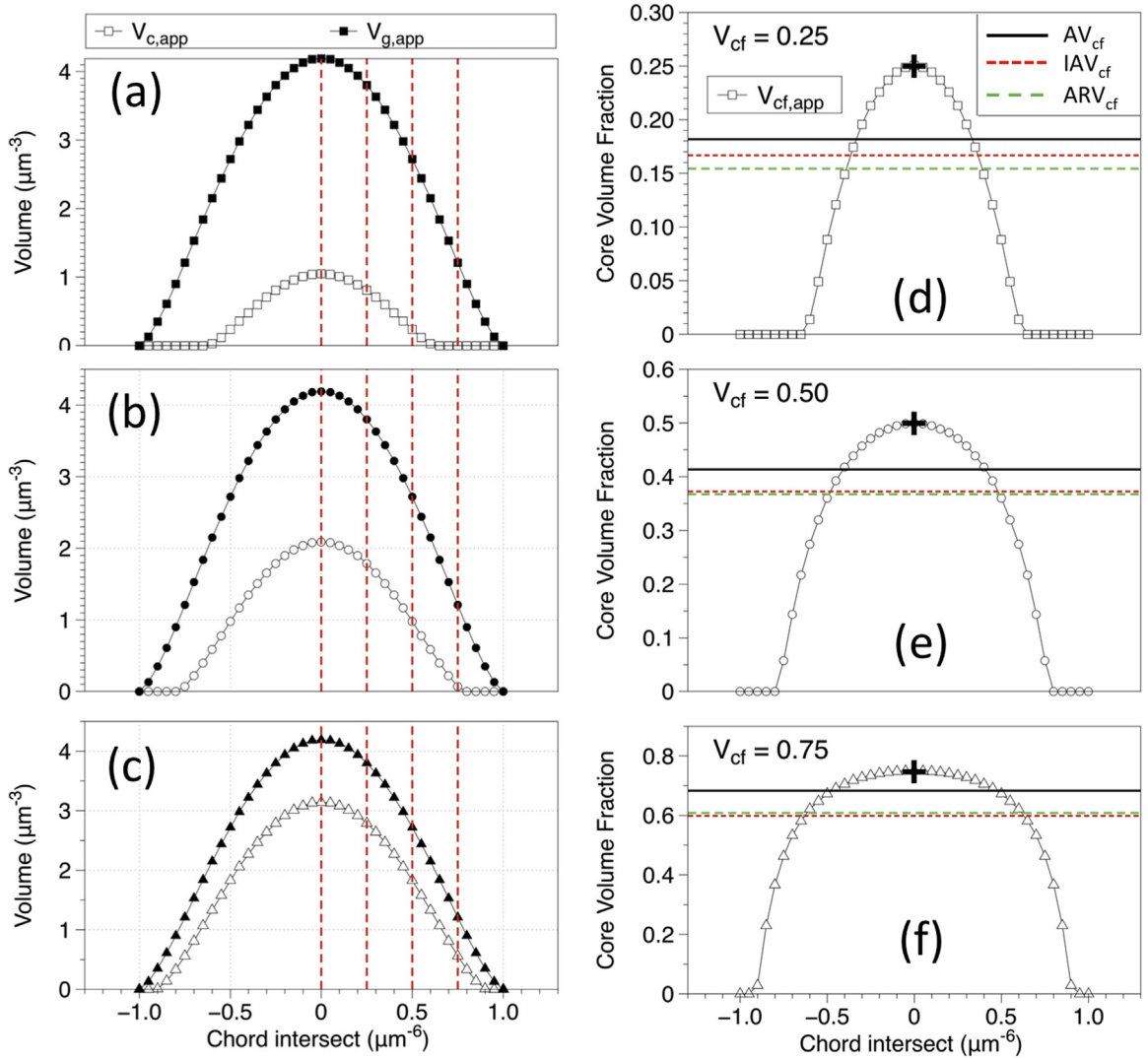

Fig. 3. Apparent grain volumes $V_{g,app}$ (closed symbols) and apparent core volumes $V_{c,app}$ (open symbols) (a, b, c) and associated apparent core-volume fractions $V_{cf,app}$ (open symbols) (d, e, f). These are measured for V_{Cf} = 0.25 (a, d), 0.50 (b, e) and 0.75 (c, f). The dashed red-lines on (a, b, c) indicate chords set at 0.00, 0.25, 0.50 and 0.75 µm corresponding to the placements (i–iv) in Fig. 2a. The horizontal lines on (d, e, f) represent the three average methods, AV_{Cf}, IAV_{Cf} and ARV_{Cf} calculated based on 100 equally spaced slices from chord intersect between −1 and +1, while the black cross highlights a cut exactly through the centre of the system that provides the true core volume fraction V_{cf} of the grain.

2. Averaging methods for calculating V_{Cf}

There are three main averaging methods to establish V_{Cf} from 2D slice images. These are: (i) the average core-volume fraction (AV_{Cf}); (ii) the individual core-volume fraction average (IAV_{Cf}); and (iii) the average radius core-volume fraction (ARV_{Cf}). These methods assume the grain and grain core are nested spheres with the core located centrally within the grain. Based on Eq. (1), we can expand this expression using these assumptions to give Eq. (3). This simplifies V_{Cf} to the ratio of the cube of the core radius r_c to the cube of the grain radius r_g,

$$V_{Cf} = \frac{V_c}{V_g} = \frac{\frac{4}{3}\pi r_c^3}{\frac{4}{3}\pi r_g^3} = \frac{r_c^3}{r_g^3} \tag{3}$$

Using Eq. (3), the values of individual grains can be averaged in different ways.

(i) The AV_{Cf} method.

The first method is to measure the individual grain size and core radius for each grain. The individual grains/core volumes are calculated, summed over the number of grains measured, n, and averaged to give

$$AV_{Cf} = \frac{\frac{1}{n}\sum_{i=1}^{n}\frac{4\pi}{3}\cdot {}_i r_c^3}{\frac{1}{n}\sum_{i=1}^{n}\frac{4\pi}{3}\cdot {}_i r_g^3} = \frac{\sum_{i=1}^{n} {}_i r_c^3}{\sum_{i=1}^{n} {}_i r_g^3} \tag{4}$$

• The IAV_{Cf} method.

The second method measures the same values but calculates the core-volume fraction of each grain first. This fraction is then summed over n grains and averaged to give

$$IAV_{Cf} = \left(\frac{1}{n}\right)\sum_{i=1}^{n}\left(\frac{\frac{4\pi}{3}\cdot {}_i r_c^3}{\frac{4\pi}{3}\cdot {}_i r_g^3}\right) = \left(\frac{1}{n}\right)\sum_{i=1}^{n}\left(\frac{{}_i r_c^3}{{}_i r_g^3}\right) \tag{5}$$

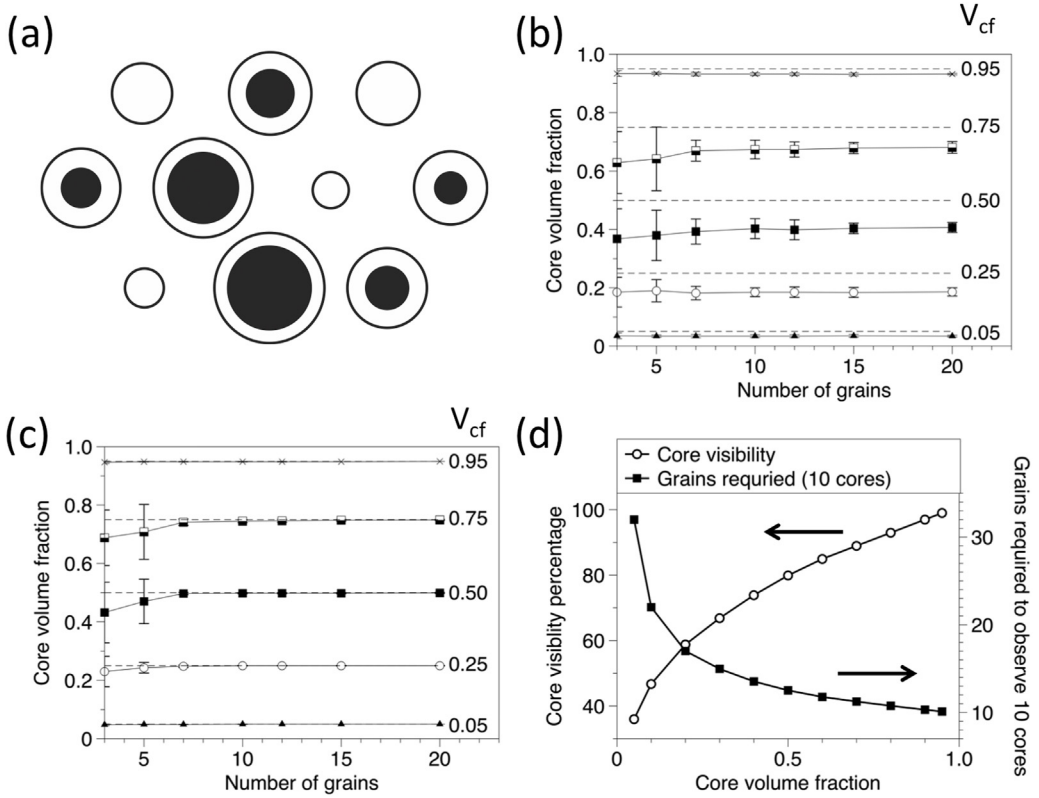

Fig. 4. The comparison between AV_{Cf} and $V_{Cf,max}$ averaging methods. (a) Ten randomly cut grains of $V_{Cf} = 0.5$ are shown. (b) The core-volume fraction using the AV_{Cf} method compared against (c) the $V_{Cf,max}$ method. Dashed lines indicate the true core-volume fraction of the model (d). Probability of core-shell visibility as a function of V_{Cf}. Also shown is the number of grains required to observe 10 core-shell structures.

- The ARV_{Cf} method.

The third method averages the individual core and grain radii separately. These average core and grain values are then used to calculate the core-volume fraction to give

$$ARV_{Cf} = \left[\frac{\left(\frac{1}{n}\right)\left\{\frac{4\pi}{3}\cdot\left(\sum_{i=1}^{n}\left({}_{i}r_{c}\right)\right)^{3}\right\}}{\left(\frac{1}{n}\right)\left\{\frac{4\pi}{3}\cdot\left(\sum_{i=1}^{n}\left({}_{i}r_{g}\right)\right)^{3}\right\}} \right] = \left[\frac{\left(\sum_{i=1}^{n}\left({}_{i}r_{c}\right)\right)^{3}}{\left(\sum_{i=1}^{n}\left({}_{i}r_{g}\right)\right)^{3}} \right] \quad (6)$$

Each method leads to slightly different values of the core-volume fraction for the same systems as demonstrated in Fig. 1. As the grains are irregular in shape and size, ImageJ [29] was used to measure two orthogonal directions through each grain centre. These values were averaged and used in Eqs. (4)–(6). The core-volume fractions for Fig. 1 are 0.33, 0.34 and 0.32 using the AV_{Cf}, IAV_{Cf} and ARV_{Cf} methods, respectively. Although these values are in good agreement, the individually calculated V_{Cf} values exhibiting a clear core-shell structure range from a minimum of 0.18 to a maximum of 0.53. This spread in V_{Cf} values leads to doubts about using this method of measurement and whether such averaging methods are appropriate.

Given the importance of the core-volume fraction in controlling the ε_r–T profile in $BaTiO_3$-based MLCCs this article addresses the question: *can 2D TEM micrographs be used to provide a reliable estimate of the core-volume fraction in core-shell microstructures of polycrystalline ceramics, and if so, what is the most reliable method?*

3. Simple spherical model

To observe the effect of averaging across all grains, we first look at a simple spherical model of a core-shell microstructure. To begin, we generate a grain by creating a sphere with a fixed radius of 1 μm. Within this volume, a smaller (black) sphere is placed centrally to represent the core. Fixing the smaller sphere radius to 0.75 μm produces a $V_{Cf} = 0.50$ as shown in Fig. 2a. The grain is then sliced using a set of chords placed at various distances from the centre of the sphere as shown in Fig. 2(a). To highlight the significance of the position of the chords we use four locations; (i) 0.00, (ii) 0.25, (iii) 0.50 and (iv) 0.75 μm with respect to the centre of the system. Each chord provides a 2D projection of the 3D structure shown in Fig. 2b–2d for three V_{Cf} values of (b) 0.25, (c) 0.50 and (d) 0.75. The radii of the various structures can then be measured allowing the apparent volume of the grain, $V_{g,app}$, and the apparent volume of the core, $V_{c,app}$ (shown in black) to be calculated to determine the apparent core-volume fraction, $V_{Cf,app}$ (based on Eq. (1)) as a function of chord intersection.

$V_{c,\,app}$ (open symbols) and $V_{g,app}$ (closed symbols) as a function of chord intersect are shown for $V_{Cf} = 0.25$, 0.50 and 0.75 in Fig. 3 a–c, respectively. As expected, the apparent grain size decreases the further the chord is from the centre. This arises from the curvature of the grain. Furthermore, if the core-volume fraction is low (e.g. $V_{Cf} = 0.25$) and the chord is sufficiently far away from the centre of the grain (e.g. 0.75 μm), the grain appears as a single material, for example Fig. 2b(iv). This is due to the chord not intersecting the core material, leaving a grain that 'appears' to have no core-shell structure.

$V_{Cf,\,app}$ (open symbols) as a function of chord intersect is shown for $V_{Cf} = 0.25$, 0.50 and 0.75 in Fig. 3d–f, respectively. As the chord begins to intersect the core, $V_{Cf,app}$ is underestimated due to the

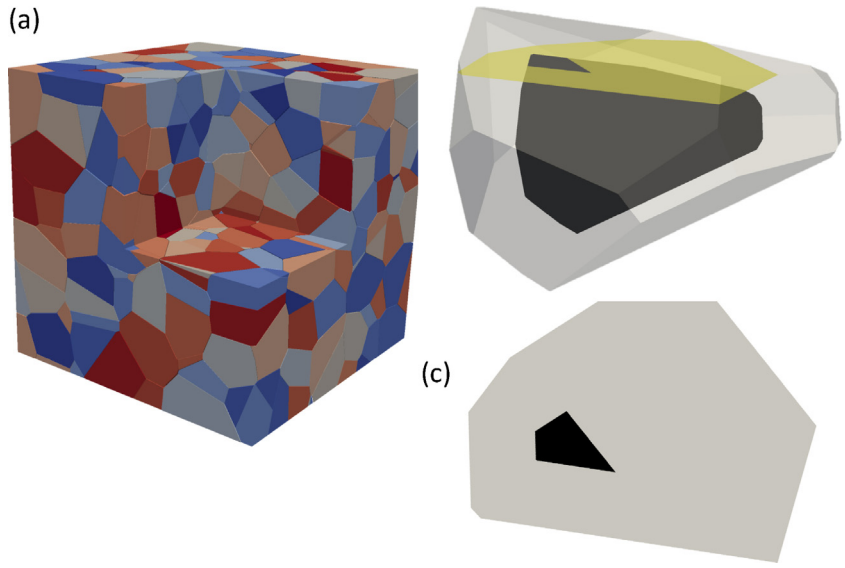

Fig. 5. (a) A randomly generated 3D polycrystalline microstructure using Voronoi tessellation. (b) An irregular shaped grain (V_{Cf} = 0.25) showing the core (black) the shell (off-white). A random slice taken through the grain is highlighted by the yellow plane. (c) The associated 2D grain projection of the slice from (b).

Table 1
The likelihood of observing 10 core-shell structures from various values of V_{Cf}. This provides the number of grains typically required to produce 10 core-shell structures and the difference in results for the AV_{Cf} averaging method compared to the $V_{Cf,max}$ method when applied to the system.

Core-volume Fraction V_{Cf}	Percentage of observing 10 core-shell structures	Number of grains required to observe 10 core-shell structures	AV_{Cf} averaging method	$V_{Cf,max}$ averaging method
0.05	36	32	0.03	0.05
0.10	47	22	0.07	0.10
0.20	59	17	0.14	0.20
0.25	64	16	0.19	0.25
0.30	67	15	0.22	0.30
0.40	74	14	0.31	0.40
0.50	80	13	0.40	0.50
0.60	85	12	0.51	0.60
0.70	89	11	0.62	0.70
0.75	91	11	0.68	0.75
0.80	93	11	0.74	0.80
0.90	97	10	0.86	0.90
0.95	99	10	0.93	0.95

differences in curvature of the shell and core surfaces. Only when the chord passes close to the centre of the grain does the 2D projection approximate to the expected V_{Cf} value. For example, $V_{Cf,app} = V_{Cf} = 0.50$ when cut through the centre of the grain but reduces to 0.06 when cut at 0.75 μm from the centre, Fig. 3e. AV_{Cf}, IAV_{Cf} and ARV_{Cf} for the same V_{Cf} values are shown as horizontal lines in Fig. 3d–f and have been averaged from 100 equally spaced cuts across the chord range from −1.00 to +1.00. As most cuts underestimate the core-volume fraction, all three averaging methods consistently underestimate V_{Cf}, as highlighted by the three lines in Fig. 3(d, e, f). The IAV_{Cf} and ARV_{Cf} methods lead to larger deviations than the AV_{Cf} method. For example, for $V_{Cf} = 0.50$, AV_{Cf} is estimated as 0.41 but is only 0.37 for the IAV_{Cf} and ARV_{Cf} methods. Although the AV_{Cf} method is an improvement, the difference compared to V_{Cf} is significant if used to characterise core-shell microstructures and an alternative method is necessary.

4. Maximum core-volume fraction ($V_{Cf,max}$) method

It is clear from this study that if grains are cut close to their centre, the apparent core-volume fraction extracted from the 2D slices will approach V_{Cf}. As highlighted in Fig. 3, averaging across many grains causes the grain core radius to be consistently underestimated as it always includes cores that appear much smaller with respect to V_c. A proposed alternative is to take the maximum core-volume fraction, $V_{Cf,max}$ as this best represents the cut closest to the centre of a grain. To test this scenario, we use a collection of grains with a fixed V_{Cf} and place chords randomly at distances from the centre of the grains. These are then used to form a collection of 2D plane images. Fig. 4a shows an example for $V_{Cf} = 0.50$ with the creation of 10 grains that have been cut at a random distance from their centres. In this example, four grains exhibit no core-shell structure and six have a measurable core-volume fraction. Applying the best averaging method, AV_{Cf}, on the six observable core-shell grains leads to an apparent core-volume fraction of 0.39. We repeat this 100 times to find the spread in this measurement. This is shown in Fig. 4b and performed for a range of V_{Cf}, i.e., 0.05, 0.25, 0.50, 0.75 and 0.95 along with a different number of starting grains. The values are then plotted against the number of grains that have been measured which ranges from three to twenty. It should be noted that grains with no core-shell structure are omitted from the averaging so as not to bias the result.

The variability on the apparent core-volume fraction is found to be large if only a few grain cores are visible. For example, when five grains are used with a small V_{Cf}, there is a strong chance that only three grains will exhibit a measurable core-shell structure

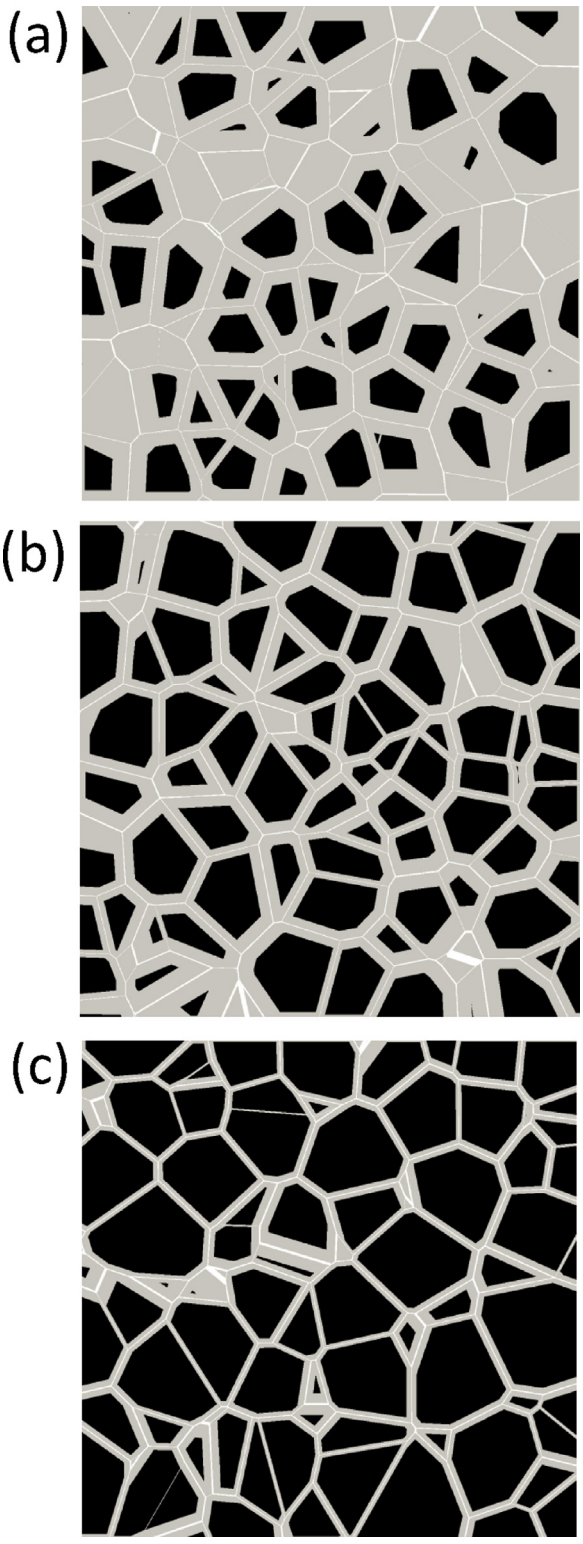

Fig. 6. Random 2D slices taken through a Voronoi generated polycrystalline microstructure. The core has been shrunk inside each grain and is based on V_{Cf} = (a) 0.25, (b) 0.50 and (c) 0.75.

along with a strong likelihood that they will all be cut away from their centres. As the number of initial grains increases, and thus the number of measurable cores increases, the apparent core-volume fraction converges with an associated reduction in the spread of values. This convergence, occurring after approximately 10 grains, is always offset from V_{Cf}. This is highlighted in Fig. 4b where the converged values do not reach the true V_{Cf} indicated by the horizontal dotted lines.

In contrast, if $V_{Cf,max}$ is extracted from the collection of grains, the core-volume fraction is found to be very close to V_{Cf}. The maximum method also converges with approximately 10 core-shell grains but to within 2% of V_{Cf} (Fig. 4c).

As a selection of randomly cut grains may not lead to the same number of core-shell grains, Fig. 4d and Table 1 estimate how many initial grains are required to generate 10 grains with visible core-shell structures. A large V_{Cf} (i.e. $\geq$0.90) leads to the core visibility being identifiably in nearly all 10 grains. As V_{Cf} decreases the probability of observing core-shell structures decreases as there are regions where the chord can cut the grain and not intersect the core. V_{Cf} = 0.50 leads to 80% of grains showing a core-shell structure. This requires thirteen grains to be confident that 10 core-shell structures are observed. This increases to over twenty grains for V_{Cf} = 0.10 as the probability falls to 47% (Table 1).

5. Polycrystalline microstructures

The maximum core-volume fraction ($V_{Cf,max}$) method has been shown to work well for a simplistic spherical model; however, ceramics are generally based on polycrystalline microstructures constructed from irregular shaped grains of various sizes. To achieve this, we employ an algorithm used in previous finite element models [30] to mimic polycrystalline samples. We distribute an array of points, representing the centres of each grain, and run Voro++ [31] to Voronoi tessellate across these points. This generates a 3D surface around each point, which is converted to a grain volume. Each grain volume can be shrunk towards its centre, creating a grain-core, and thus a core-shell-type microstructure can be generated. A random distribution of seed points is used to produce a varied grain size, where each grain possesses a unique shape as shown in Fig. 5a. Due to the irregular 3D grain shape, it is possible that the grain cores do not appear centralised in this model and that they 'appear' in a 2D slice as a very different shape to the actual 3D grain. An example of such an irregular grain is shown in Fig. 5b and the resulting 2D slice of an asymmetrical core-shell structure shown in Fig. 5c.

It is challenging to determine the core-volume fraction of these irregular 3D grains in polycrystalline microstructures as the size of the grain and the associated core become dependent on the direction of the line scan and are prone to large errors. As these grains are generated from slices away from the centre of the grain they will always underestimate the core-volume fraction and so do not feature in the final result of the $V_{Cf,max}$ method.

To verify the $V_{Cf,max}$ method on realistic polycrystalline microstructures, 10 models using randomised seed points were made for V_{Cf} = 0.25, 0.50 and 0.75. Each model was randomly cut to provide 2D projections of the polycrystalline microstructures, examples of which are shown in Fig. 6. Based on the simple spherical grain model, Table 1 lists how many randomly selected initial spherical grains are required to perform an analysis and this was applied to the polycrystalline microstructures; e.g. sixteen grains are required for V_{Cf} = 0.25, Fig. 6b. Using the AV_{Cf} method on these grains produces an apparent core-volume fraction variation across the 10 randomised models ranging from 0.03 to 0.20. These values possess a large degree of uncertainty due to the significant number of asymmetric grain-core structures generated. Using the $V_{Cf,max}$ method on the same selected grains, the values range between 0.24 and 0.25, marking a significant improvement. Results for the other two V_{Cf} values follow the same trend as shown in Table 2. These results highlight the significant improvement of using the $V_{Cf,max}$ method over the AV_{Cf} method for polycrystalline microstructures. There is also increased confidence and repeatability from this

Table 2
Comparison of the AV_{Cf} and $V_{Cf,max}$ methods measured over 10 randomly generated polycrystalline microstructures.

V_{Cf}	AV_{Cf} range	$V_{Cf,max}$ range
0.25	0.03–0.20	0.24–0.25
0.50	0.20–0.25	0.48–0.49
0.75	0.50–0.61	0.72–0.74

method as the results are not dependent on the asymmetry of the grains.

6. Conclusions

Understanding how the core-volume fraction is modified during processing is of critical importance for improving present generation MLCCs and next generation, RE-free material alternatives. The analysis and direction of how to modify the chemistry and processing to optimise the core-shell microstructure relies on accurate core-shell volume fractions typically performed on TEM micrographs by measuring the microstructure either by EDX or by contrast changes.

Using an analytical approach we have showed how averaging the core and shells microstructures that are visible in a TEM micrograph does not reduce the error in measuring the core-volume fraction but will consistently underestimate the value calculated. This error exists on the simplistic spherical model and the realistic polycrystalline core-shell microstructures. It arises from cutting grains away from the centre such that they exhibit a lower apparent core-volume fraction than the true value.

Instead of averaging across all the grains present in a TEM micrograph, we show that taking ten core-shell grains and extracting the maximum core-volume fraction from these can lead to significance improvements in accuracy and confidence. This ratio best represents the cut closest to the centre of a grain and therefore the true core-volume fraction.

The error in averaging can be significant. Returning to the TEM micrograph presented in Fig. 1 we showed how the different averaging methods agreed, indicated a core-volume ratio of approximately 0.33, suggesting the core-volume material is one-third of the total grain volume. Using the $V_{Cf,max}$ method on grains with a visible core-shell structure, this value increases to 0.5. This suggests an error of 17% in the core-volume and in the example the core component is actually 50% of the total grain volume. This strongly suggests that previous estimates of core-shell volume fractions using simple averaging methods in the literature have significantly underestimated the core-volume fraction in core-shell microstructure ceramics.

Acknowledgements

We thank AVX Ltd for supplying MLCC capacitors, and EPSRC for financial support on the Sustainability and Substitution of Functional Materials and Devices grant (EP/L017563/1).

References

[1] S. Agarwal, Reliability of multilayer ceramic capacitors with base-metal electrodes, EEE Parts Bull. 5 (2) (2013).
[2] Global and Chinese multi-layer ceramic capacitor (MLCC) industry report - 2015-2018. ID: 3495932, 2015.
[3] S. Hoenderdaal, L.T. Espinoza, F. Marscheider-Weidemann, W. Graus, Can a dysprosium shortage threaten green energy technologies? Energy 49 (2013) 344–355.
[4] J. Ho, T.R. Jow, S. Boggs, Historical introduction to capacitor technology, IEEE Electr. Insulat. Mag. 26 (1) (2010) 20–25.
[5] Murata - chip monolithic ceramic capacitors http://www.murata.com/~/media/webrenewal/support/library/catalog/products/capacitor /mlcc/c02e.ashx (accessed 1/11/15).
[6] C.-H. Kim, K.-J. Park, Y.-J. Yoon, M.-H. Hong, J.-O. Hong, K.-H. Hur, Role of yttrium and magnesium in the formation of core-shell structure of $BaTiO_3$ grains in MLCC, J. Eur. Ceram. Soc. 28 (6) (2008) 1213–1219.
[7] C.-C. Chou, C.-S. Chen, I.N. Lin, W.-C. Yang, H.-F. Cheng, Development of X7R type base-metal-electroded $BaTiO_3$ capacitor materials by co-doping of MgO/Y_2O_3 additives, Ferroelectrics 332 (2006) 35–39.
[8] J. Nishikawa, T. Hagiwara, K. Kobayashi, Y. Mizuno, H. Kishi, Effects of microstructure on the curie temperature in $BaTiO_3$-Ho_2O_3-MgO-SiO_2 system, Jpn. J. Appl. Phys., Part 1 46 (10B) (2007) 6999–7004.
[9] K.-J. Park, C.-H. Kim, Y.-J. Yoon, S.-M. Song, Y.-T. Kim, K.-H. Hur, Doping behaviors of dysprosium, yttrium and holmium in $BaTiO_3$ ceramics, J. Eur. Ceram. Soc. 29 (9) (2009) 1735–1741.
[10] J.S. Dean, P.Y. Foeller, I.M. Reaney, D.C. Sinclair, A resource efficient design strategy to optimise the temperature coefficient of capacitance of $BaTiO_3$-based ceramics using finite element modelling, J. Mater. Chem. A 4 (18) (2016) 6896–6901.
[11] S.-C. Jeon, B.-K. Yoon, K.-H. Kim, S.-J. Kang, Effects of core/shell volumetric ratio on the dielectric-temperature behavior of $BaTiO_3$, J. Adv. Ceram. 3 (1) (2014) 76–82.
[12] P.Y. Foeller, J.S. Dean, I.M. Reaney, D.C. Sinclair, Design of a bilayer ceramic capacitor with low temperature coefficient of capacitance, Appl. Phys. Lett. 109 (8) (2016) 082904.
[13] D. Maurya, F.C. Sun, S.P. Alpay, S. Priya, A new method for achieving enhanced dielectric response over a wide temperature range, Sci. Rep. UK 5 (2015) 15144.
[14] D.C. Sinclair, A.R. West, Impedance and modulus spectroscopy of semiconducting $BaTiO_3$ showing positive temperature-coefficient of resistance, J. Appl. Phys. 66 (8) (1989) 3850–3856.
[15] A.R. West, D.C. Sinclair, N. Hirose, Characterization of electrical materials, especially ferroelectrics, by impedance spectroscopy, J. Electroceram. 1 (1) (1997) 65–71.
[16] N.J. Kidner, N.H. Perry, T.O. Mason, E.J. Garboczi, The brick layer model revisited: introducing the nano-grain composite model, J. Am. Ceram. Soc. 91 (6) (2008) 1733–1746.
[17] J.P. Heath, J.S. Dean, J.H. Harding, D.C. Sinclair, Simulation of impedance spectra for core-shell grain structures using finite element modeling, J. Am. Ceram. Soc. 98 (6) (2015) 1925–1931.
[18] L. Holzer, F. Indutnyi, P.H. Gasser, B. Munch, M. Wegmann, Three-dimensional analysis of porous $BaTiO_3$ ceramics using FIB nanotomography, J. Microsc. Oxford 216 (2004) 84–95.
[19] Z.L. Yan, O. Guillon, C.L. Martin, S. Wang, C.S. Lee, F. Charlot, D. Bouvard, Correlative studies on sintering of Ni/$BaTiO_3$ multilayers using X-ray computed nanotomography and FIB-SEM nanotomograhy, J. Am. Ceram. Soc. 98 (4) (2015) 1338–1346.
[20] M.M. Samantaray, K. Kaneda, W. Qu, E.C. Dickey, C.A. Randall, Effect of firing rates on electrode morphology and electrical properties of multilayer ceramic capacitors, J. Am. Ceram. Soc. 95 (3) (2012) 992–998.
[21] Z. Tian, X. Wang, H. Gong, T.-H. Song, K.H. Hur, L. Liz, Core-shell structure in nanocrystalline modified $BaTiO_3$ dielectric ceramics prepared by different sintering methods, J. Am. Ceram. Soc. 94 (4) (2011) 973–977.
[22] C.-H. Kim, K.-J. Park, Y.-J. Yoon, J.-O. Hong, D.-S. Sinn, K.-H. Hur, Ieee, Formation of core-shell structure of $BaTiO_3$ grains in MLCC, 2007. Sixteenth IEEE International Symposium on the Applications of Ferroelectrics, vols 1 and 22007, pp. 540–543.
[23] S.-C. Jeon, C.-S. Lee, S.-J.L. Kang, The mechanism of core/shell structure formation during sintering of $BaTiO_3$-based ceramics, J. Am. Ceram. Soc. 95 (8) (2012) 2435–2438.
[24] Z.B. Shen, X.H. Wang, D.S. Song, L.T. Li, Nb-doped $BaTiO_3$-$(Bi_{0.5}Na_{0.5})TiO_3$ ceramics with core-shell structure for high-temperature dielectric applications, Adv. Appl. Ceram. 115 (7) (2016) 435–442.
[25] Y. Liu, B. Cui, Y. Wang, R. Ma, M.Q. Shangguan, X.T. Zhao, S.H. Wang, Q.Y. Li, Y.Y. Wang, Core-shell structure and dielectric properties of $Ba_{0.991}Bi_{0.006}TiO_3$@$Nb_2O_5$-$Co_3O_4$ ceramics, J. Am. Ceram. Soc. 99 (5) (2016) 1664–1670.
[26] C.A. Randall, S.F. Wang, D. Laubscher, J.P. Dougherty, W. Huebner, Structure property relationships in core-shell $BaTIO_3$-LiF ceramics, J. Mater. Res. 8 (4) (1993) 871–879.
[27] H.Y. Lu, J.S. Bow, W.H. Deng, Core-shell structures in ZrO_2-modified $BaTiO_3$ ceramic, J. Am. Ceram. Soc. 73 (12) (1990) 3562–3568.
[28] C.-H. Kim, K.-J. Park, Y.-J. Yoon, D.-S. Sinn, Y.-T. Kim, K.-H. Hur, Effects of milling condition on the formation of core-shell structure in $BaTiO_3$ grains, J. Eur. Ceram. Soc. 28 (13) (2008) 2589–2596.
[29] C.A. Schneider, W.S. Rasband, K.W. Eliceiri, NIH image to imageJ: 25 years of image analysis, Nat. Methods 9 (7) (2012) 671–675.
[30] J.S. Dean, J.H. Harding, D.C. Sinclair, Simulation of impedance spectra for a full three- dimensional ceramic microstructure using a finite element model, J. Am. Ceram. Soc. 97 (3) (2014) 885–891.
[31] C.H. Rycroft, VORO plus plus: a three-dimensional voronoi cell library in C plus, Chaos 19 (4) (2009).